Multi-Scale Study of the Influence of Bonding Temperature on the Diffusion Bonding of Equiatomic CoCrFeMnNi High Entropy Alloy and 316L Stainless Steel

Olushola Bamidele Nenuwa, Léo Thiercelin, Laurent Peltier, Eric Fleury, Nathalie Siredey-Schwaller, Adil Benaarbia

Multi-Scale Study of the Influence of Bonding Temperature on the Diffusion Bonding of Equiatomic CoCrFeMnNi High Entropy Alloy and 316L Stainless Steel

Olushola Bamidele Nenuwa[1,3] · Léo Thiercelin[1] · Laurent Peltier[1] · Eric Fleury[1] · Nathalie Siredey-Schwaller[1] · Adil Benaarbia[2]

Abstract

The microstructural evolution and mechanical characteristics of CoCrFeMnNi high entropy alloy (HEA) joined to 316 L stainless steel (SS316L) were investigated by performing diffusion bonding at temperatures ranging from 975 °C to 1050 °C under a compressive pressure of 5 MPa. The diffusion-bonded samples were examined microstructurally with a Scanning Electron Microscope (SEM) equipped with an Energy Dispersive Spectrometer (EDS), Electron Back Scattered Diffraction (EBSD) and X-ray Diffraction (XRD) analyses, and the mechanical responses of the joints were assessed based on the fracture energy calculation from the shear test results. The CoCrFeMnNi-HEA was successfully joined to SS316L preserving a single face centred cubic (FCC) phase solid solution within the diffusion zone. Increasing the bonding temperature led to widening the diffusion zones and microstructural changes such as grain growth, which became more prominent, particularly for temperatures equal to 1025 °C and beyond. The optimum bonding temperature was observed to be 1000 °C, corresponding to a total diffusion width of 10.5 µm. These diffusion joints were characterised by the moderate presence of interfacial pores and the highest fracture energy.

Keywords Diffusion bonding · Fracture energy · High entropy alloy (HEA) · Microstructural characterisation · Stainless steel

1 Introduction

In 2004, Brian Cantor [1] and Yeh [2] presented a new class of materials called "high entropy alloys" (HEAs), which are solid-solution alloys containing at least five or more principal alloying elements in an equiatomic or near-equiatomic composition. Over the last two decades, there has been growing interest in these alloys, which form part of the family of multi-principal element alloys or compositionally complex alloys [3–5] with remarkable physical, chemical and mechanical properties comparable to and sometimes superior to conventional alloys under extreme temperatures [6–11]. The equiatomic CoCrFeMnNi HEA, known as the "Cantor alloy", is the most studied single-phase and face-centred-cubic structured HEA [1, 12, 13, 14]. The properties of equiatomic CoCrFeMnNi high entropy alloy have been well investigated, and it is acknowledged that this material displays a combination of interesting properties such as good corrosion and irradiation resistance [15–19], as well as excellent mechanical properties (ductility, yield strength, tensile strength, fracture toughness) at room and cryogenic temperatures [20–22]. For structural applications, the weldability of the HEA is important to ensure the integrity of assemblies, which explains the emergence of this research field over the last decade. General review articles on the welding of high entropy alloys [13, 23–27] have already

✉ Adil Benaarbia
adil.benaarbia@centralelille.fr

[1] Arts et Métiers Institute of Technology, CNRS, Université de Lorraine, Metz LEM3-UMR 7239, F- 57000, France

[2] Univ. Lille, CNRS, INRAE, Centrale Lille, UMR 8207, UMET – Unité des Matériaux et Transformations, Lille F-59000, France

[3] Department of Mineral & Petroleum Resources Engineering, Federal Polytechnic, P.M.B. 5351, Ado-Ekiti, Nigeria

been dedicated to the joining of similar and dissimilar combinations of HEAs and other alloys.

The weldability of similar CoCrFeMnNi HEA has been investigated using Laser beam welding, electron beam welding, and gas tungsten arc welding [28–33]. Solid-state ultrasonic welding [34] and friction stir welding [28, 35] have also been conducted. Joints without solidification cracks were produced but, in most of the fusion-based welding, the fusion zones were found to be of poor resistance compared with the base metal due to microstructural heterogeneity in this region. However, this HEA alloy will be relatively more expensive than commercial alloys such as austenitic stainless steels because of the higher concentration of alloying elements. Although using HEA for full structural application seems unrealistic, dissimilar welding of FCC HEA to FCC austenitic stainless steel with near-identical properties (corrosion resistance, good ductility, toughness and strength at cryogenic temperature) could ensure better manufacturing economy and design. Dissimilar bonding of CoCrFeMnNi HEA with other materials is now gaining more attention although a majority of these studies focused on fusion-based welding such as laser beam welding [12, 36–39] and Tungsten Inert Gas (TIG) welding [40–42]. During laser welding of equatomic CoCrFeMnNi and SS316 (stainless steel with higher carbon content), Oliveira et al. [38] showed that the fusion zone was composed of a single FCC phase. Recently, Friction Stir Welding which is a solid-state joining technique, has been used to produce dissimilar joints by welding CoCrFeMnNi HEA with 304 stainless steel [41, 43] and the HEA with high-manganese austenite steel [44].

Although fusion based welding process accomplished by melting and solidification of the base metals has been extensively used, it presents the disadvantages of the formation of brittle intermetallic compounds, high welding distortion, microstructural heterogeneities and weakening of the fusion zone and heat-affected zone leading to residual stresses, which could induce cracking during solidification [24, 27]. To avoid some of these problems, diffusion bonding (DFB) is an alternative solid-state joining process with the advantage of being conducted at temperatures below the melting point of both base materials, hence minimising the presence of bonding defects and keeping good material properties. However, dissimilar diffusion bonding may cause stress at the bond interface due to a mismatch of the thermal expansion coefficient between two different base materials which could lead to the formation of micro-cracks. Moreover, the formation of new detrimental phases may occur at the bond region, which could deteriorate the mechanical behaviour and the fracture toughness of the joints [45].

To the authors' knowledge, only a few studies were conducted on the dissimilar diffusion bonding with CoCrFeMnNi HEA. Liu has investigated the diffusion bonding of equiatomic CoCrFeMnNi and pure copper [46]. Recently, equiatomic CoCrFeMnNi HEA and some of its medium entropy alloy subsystems were joined by diffusion bonding to 316 stainless steel [47] using a spark plasma sintering device. These authors studied the effect of bonding temperature on the diffusion of elements and tensile properties of bonded joints. It was observed that the tensile strength of the joints improved as the bonding temperature increased, with the optimal bonding temperature for all joints being 80% of the melting point of the lower base materials. This was primarily due to a reduction in porosity formation. In fact, with this technique, porosities tend to occur at the bond interfaces over a wide range of temperatures. Diffusion bonding of equiatomic CoCrFeMnNi HEA and 304 stainless steel was conducted [48] by first obtaining nanocrystalline grains in the HEA via Surface Mechanical Attrition Treatment (SMAT). It was reported that the detrimental brittle phase and Kirkendall porosity were not observed and that the distance of diffusion of Fe atoms increased significantly with an increase in the SMAT time. The joint attained an enhanced shear strength of 320 MPa at a lower bonding temperature of 850 °C, which was attributed to the SMAT processing since this method not only induced a reduction of the grain size of the HEA but also introduced more grain boundaries that served as diffusion channels. Moreover, this technique is associated with an increase in the dislocation density in the sub-surface of CoCrFeMnNi.

The focus of this work was to conduct diffusion bonding between equiatomic CoCrFeMnNi HEA and 316 L stainless steel at different bonding temperatures and to investigate the influence of this varying parameter and the high entropy effect on the properties of the final bonded samples. Equiatomic CoCrFeMnNi-HEA was elaborated and joined to the SS316L by diffusion bonding at different temperatures during the same bonding time. The microstructures were first analysed by X-ray Diffraction (XRD), and diffusion mechanisms of the bonded assemblies were examined using a Scanning Electron Microscope equipped with an Energy Dispersive Spectrometer (SEM-EDS) and Electron Back-Scattered Diffraction (EBSD). The diffusion chemical profiles were analysed to establish the diffusion zones and to determine the diffusion coefficients of the major elements across the bond interfaces of the various assemblies. Fick's second law of diffusion was used to compute the diffusion coefficients. In comparison to classical analysis, values of the diffusion coefficients were computed for each element in the parent materials on both sides of the diffusion joint. The mechanical responses of the bonded samples were assessed based on the fracture energy obtained from the shear test results.

Table 1 Chemical composition of the SS316L and CoCrFeMnNi HEA

Element	Co	Cr	Fe	Mn	Ni	Mo
SS316L (wt%)	0.16	16.70	68.80	1.38	10.00	2.00
SS316L (at%)	0.15	17.85	68.45	1.40	9.47	1.16
HEA (wt%)	20.72	18.84	20.01	19.15	21.28	-
HEA (at%)	19.72	20.30	20.09	19.55	20.33	-

Table 2 Diffusion bonding conditions of the SS316L-CoCrFeMnNi joints (T_m is the Liquidus temperature of CoCrFeMnNi-HEA = 1602 K)

Bonding temperature (K)	Equivalence	Pressure (MPa)	Time (min)
1248 (975 °C)	0.78 T_m	5	60
1273 (1000 °C)	0.79 T_m	5	60
1298 (1025 °C)	0.81 T_m	5	60
1323 (1050 °C)	0.83 T_m	5	60

2 Experimental Procedures

2.1 Materials Preparation

Equiatomic CoCrFeMnNi HEA alloy was produced by vacuum induction melting of its constituent pure elements (purity ≥ 99.9 wt%) using a cold crucible. The vacuum induction furnace was operated under a controlled environment of high-purity argon (Ar) to prevent elemental oxidation. The ingot was remelted five times to improve the compositional homogeneity of the alloy before it was drop cast into a mould to produce a 20 mm × 20 mm × 27 mm parallelepipedic ingot. To eliminate solidification structures and ensure further homogenisation of the alloy, the ingot was heat-treated at a temperature of 1200 °C for 24 h and then cooled by water quenching. The CoCrFeMnNi sample obtained was finally cut into cubes of 5 x 5 x 5 mm^3 dimensions. 316 L stainless steel plate of 10 mm thickness was commercially sourced and its chemical composition was examined by the spark optical emission spectrometer in a previous work [49]. The SS316L sample was also cut into cubes with dimensions of 10 x 10 x 10 mm^3. The chemical composition of the main elements in the SS316L and that of the HEA is shown in Table 1. The other elements in SS316L are C (0.03 wt%), Si (0.34 wt%), P (0.03 wt%), S (0.003 wt%), Cu (0.37 wt%), Ti (0.007 wt%), V (0.07 wt%), N (0.06 wt%), W (0.06 wt%).

2.2 Implementation of Diffusion Bonding

The HEA and SS316L samples earlier cut were polished by conventional metallographic techniques to obtain mirror-like surfaces and the surfaces were cleaned with ethanol to remove contamination. The samples were assembled and finally mounted inside the diffusion bonding set-up as reported in the authors' previous work [49]. The diffusion bonding was performed at the four different bonding temperatures of 975 °C, 1000 °C, 1025 °C and 1050 °C during 60 min bonding time under a compressive pressure of 5 MPa (see Table 2). The heating rate was set at 15 °C/min to attain the expected bonding temperature. After the bonding time, the furnace was switched off and the specimens were left to slowly cool down to room temperature in the furnace. The bonding temperatures were set in proportion to the liquidus temperature of Cantor alloy which is the base material with the lowest melting point. In this work, the liquidus temperature was acknowledged as the melting temperature as it defines the temperature at which the alloy is fully in a liquid state. The liquidus temperature of the equiatomic CoCrFeMnNi alloy was measured using a Netzsch 404 C differential scanning calorimeter (DSC) and it was found to be 1329 °C. The diffusion bonding was performed at approximately 0.78 T_m, 0.79 T_m, 0.81 T_m, and 0.83 T_m, where T_m represents the liquidus temperature of Cantor alloy in degrees Kelvin (K). For reference, the melting temperature of SS316L is 1400 °C [50].

2.3 Microstructural Examination

After proper sample preparation by conventional metallographic procedures to obtain mirror-like surfaces, the microstructures of the parent alloys and bonded samples were examined in a Zeiss Supra 40 scanning electron microscope (SEM) operated at 15 kV and equipped with a Bruker X Flash 6/30 detector using the EDS technique for the chemical composition analyses. The bond interfaces revealed by the bonded samples were carefully examined with the SEM-EDS machine. An image analysis software (ImageJ 1.54d) was used for microstructural quantitative measurements based on standard test methods for determining average grain size using the standard ASTM E112. The electron backscattered diffraction (EBSD) analyses of the bonded samples were conducted with the JEOL F100 scanning electron microscope equipped with Oxford Instruments EBSD detector. The EBSD data was post-processed with the AZtecCrystal software to generate the grain orientation maps and phase maps which were used for further examination of the microstructural evolution and grain boundary diffusion of the bonded samples. The phases in the parent samples (SS316L and heat-treated HEA) and fractured bonded samples were investigated with the D8

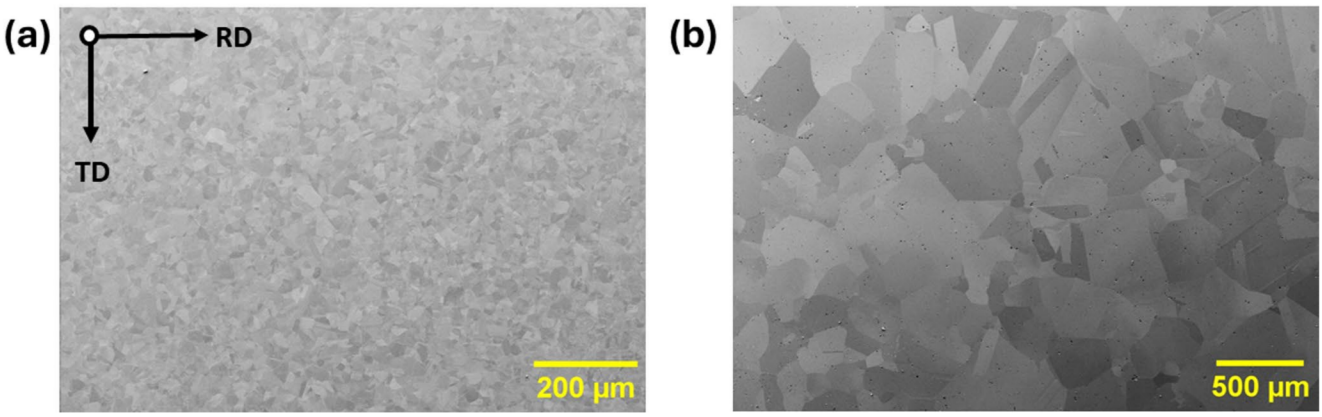

Fig. 1 Microstructure of (**a**) as-received SS316L sample taken perpendicularly to the normal direction (ND) with an average grain size of 11.8 ± 1.3 µm (**b**) as-prepared equiatomic CoCrFeMnNi HEA with an average grain size of 161.0 ± 15.3 µm

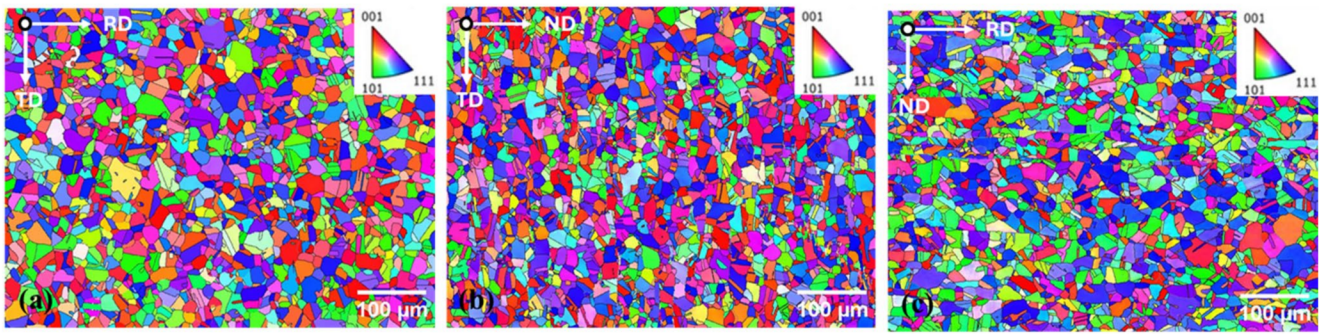

Fig. 2 EBSD orientation maps of as-received SS316L when viewed from (**a**) normal direction, (**b**) rolling direction, (**c**) transverse direction

Advance X-ray diffractometer equipped with a Co anode (λ = 1.7903 Å).

2.4 Shear Tests

Shear tests were performed on the bonded samples using the Zwick Roell Z050 uniaxial testing machine. The shear tests were conducted under displacement control at a strain rate of 0.5 mm/min until failure occurred. The fracture energy, G_f, which is the energy per unit area (J/m^2) of fracture needed to extend a crack, is calculated from the expression:

$$G_f = \frac{W_t}{A_t} \tag{1}$$

where W_t is the total work done or energy (J) to fracture the sample computed as the integral of the force-displacement curve and A_f is the cross-sectional area of the fractured surface. The shear test was not conducted on bonded samples at a temperature of 1050 °C (0.83 T_m) because several literature already reported that the most suitable temperature for conducting diffusion welding is between 0.6 T_m to 0.8 T_m, where T_m is the melting temperature in degrees Kelvin of the base material with the lowest melting point [45, 51].

3 Results

3.1 Microstructures of the Parent Samples

The micrographs obtained in the secondary electrons mode of the SEM for the as-received SS316L and heat-treated CoCrFeMnNi HEA are shown in Fig. 1. The EBSD orientation maps of the as-received SS316L viewed from three different directions are presented in Fig. 2. Equiaxed grains and several annealing twins are revealed in the as-received SS316L microstructure having an average grain size of 11.8 ± 1.3 µm. SS316L is a material with low stacking fault energy [52], therefore it is expected that the thermo-mechanical history of hot rolling, solution annealing and water quenching would have introduced several twins. The heat-treated CoCrFeMnNi HEA has much larger grains compared to that of SS316L with an average size of 161 ± 15.3 µm. The EBSD orientation maps of SS316L (Fig. 2) showed various grains oriented in different directions. Figure 2a displayed full grains across the microstructure when viewed from the normal direction (ND) while Fig. 2b – c revealed some truncated grains when viewed from the rolling direction (RD) and transverse direction (TD). These truncated

grains can be attributed to the rolling history of the SS316L during manufacturing.

3.2 X-ray Diffraction Patterns of Parent Samples

Figure 3 displays the X-ray diffraction patterns of the parent alloys (SS316L and CoCrFeMnNi-HEA). In all the patterns, only the three peaks corresponding to the {111}, {200} and {220} family planes are observed, indicating the presence of a single FCC crystal structure. For SS316L, austenite is the only FCC phase present, and the relative intensity of the (111) and (200) peaks suggests a moderate crystalline texture. The values of the lattice parameter, "a" for SS316L is 3.601 ± 0.002 Å and that of CoCrFeMnNi HEA is 3.614 ± 0.001 Å.

3.3 Microstructural Characteristics of the Bonded Samples

3.3.1 Microstructures at Various Bonding Temperatures

The microstructures of the joints bonded were observed for the different diffusion bonding temperatures to evaluate the quality of the bonding. A qualitative assessment of the diffusion-bonded joints as revealed by SEM operated in the back-scattered electron (BSE) mode is presented in Fig. 4. Low-magnification micrographs are displayed on the left side in Figs. 4a, c, e & g while the corresponding micrographs at higher magnification are shown in Figs. 4b, d, f & h. Further assessment of these micrographs with the Image J software provided the quantitative results summarized in Table 3.

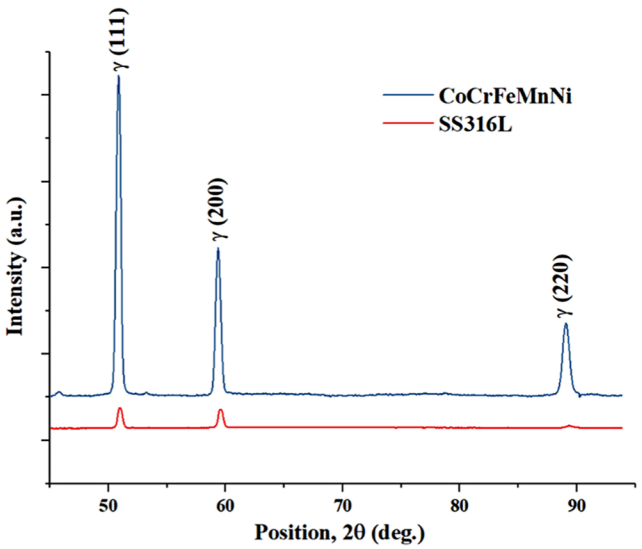

Fig. 3 XRD patterns of the parent materials: commercial SS316L and heat-treated CoCrFeMnNi HEA samples. X-ray was from a cobalt tube source (λ = 1.7903Å)

Figure 4a – b are the microstructures of the assembly bonded at a temperature of 975 °C, which is equivalent to $0.78T_m$. The low magnification microstructure showed obvious material continuity across the bond interface without any visible crack in the joint while the microstructure at higher magnification was characterised by some microvoids. The interfacial pore size is below 0.1 µm and the pore fraction is only 2%. After bonding, the SS316L grains did not present any noticeable changes in either morphology or sizes (see Table 3) but the CoCrFeMnNi grains near the bond interface were seriously deformed (Fig. 4a). The HEA grains far away from the bond interface did not also change significantly as compared to their sizes before bonding. The distorted CoCrFeMnNi grains near the interface may be attributed to accumulated residual stresses that were not completely relieved due to low bonding temperatures.

The microstructures of the samples bonded at a temperature of 1000 °C ($0.79T_m$) as shown in Fig. 4c – d displayed joints of good quality between the parent materials with a few microvoids and interfacial pores that are not very visible even when observed at higher magnification. The bonding quality is excellent, as the interfacial pore size is less than 0.1 µm, with a pore volume fraction of 1.9%. The average sizes of the SS316L and CoCrFeMnNi grains did not change significantly after bonding. However, there was no distortion of the CoCrFeMnNi grains near the bond interface as observed at 975 °C, which may be due to stress relaxation via diffusion, which helps to redistribute the stresses.

At the bonding temperature of 1025 °C ($0.81T_m$), the microstructures presented in Fig. 4e - f were also characterised by good joints with interfacial pore size below 0.5 µm. However, the bonding quality in this case is lower as the interfacial pore fraction is 12.7%. The SS316L and HEA grain sizes before and after bonding were almost similar. When the base samples were bonded at temperatures of 1050 °C ($0.83T_m$), the quality of the joint further deteriorated as the fraction of interfacial pore increased to 23.1% and the pore size became larger up to 1 µm. Coarsening of the SS316L grains near the bond interface became prominent and their sizes became four times larger than that of the as-received SS316L (the average size of the coarse grains is 43.4–47.9 µm). The yellow dashed lines highlight the boundary of grain coarsening, the width of this boundary from the bond interface for the joint bonded at 1050 °C is 202.4 ± 32.1 µm. It is important to note that the SS316L grains beyond the grain coarsening boundaries did not significantly change after bonding.

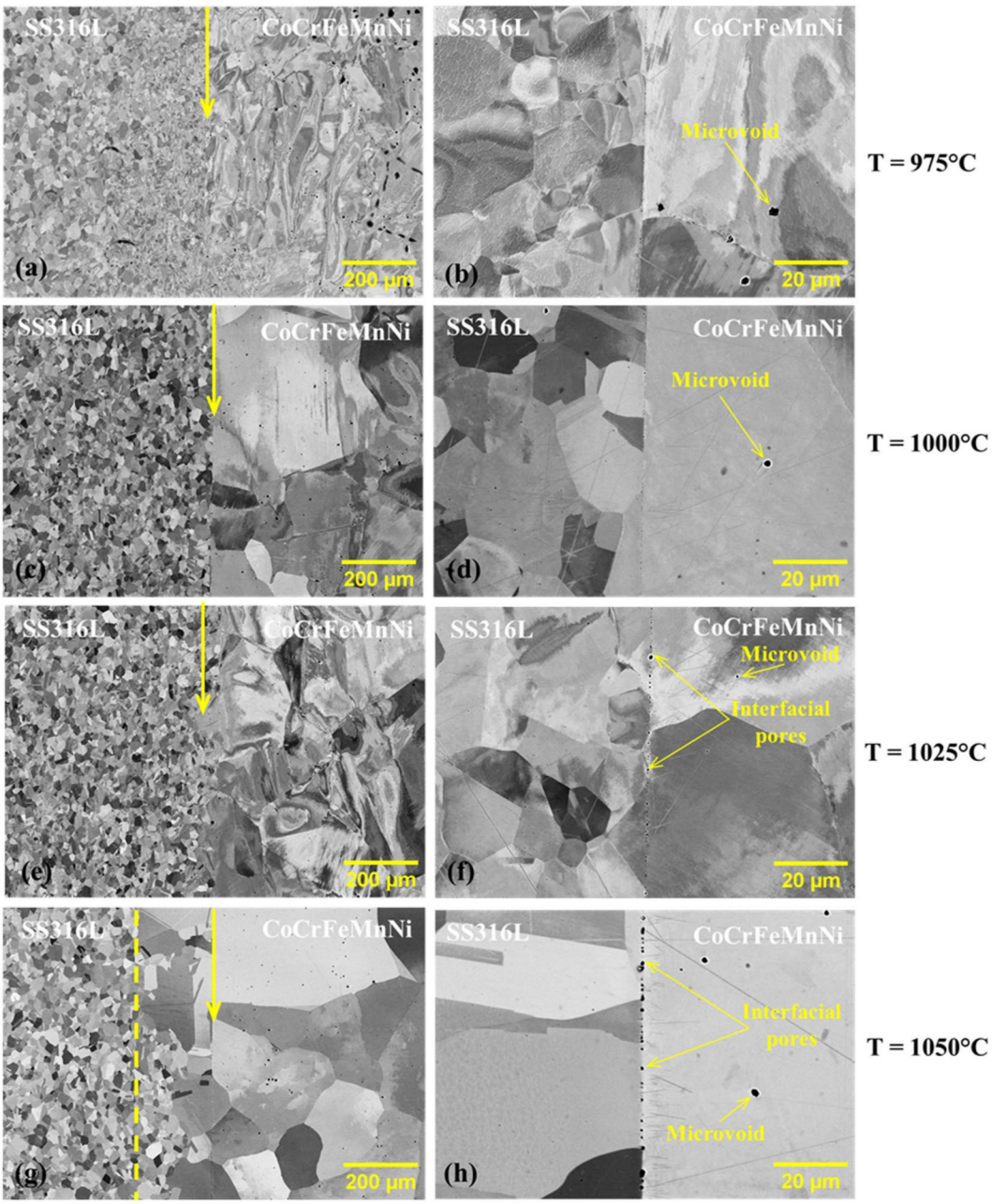

Fig. 4 SEM micrographs at low and high magnifications of the SS316L-CoCrFeMnNi joints bonded at temperatures of: (**a**, **b**) 975 °C, (**c**, **d**) 1000 °C, (**e**, **f**) 1025 °C, (**g**, **h**) 1050 °C (Thick yellow arrows in the microstructures on the left indicate the locations of the bond interfaces)

Table 3 Summary of quantitative parameters measured using ImageJ within the microstructure of the diffusion-bonded samples at various bonding temperatures

Bonding temperature (°C)	Average size of SS316L coarse grains (µm)	Average size of SS316L fine grains (µm)	Grain size of HEAs (µm)	Average size of interfacial pore (µm)	Interfacial pore fraction (%)
975	-	10.3 ± 2.5	164.7 ± 21.4	< 0.1	2.0
1000	-	10.2 ± 1.3	164.7 ± 37.3	< 0.1	1.9
1025	-	10.5 ± 2.9	165.2 ± 37.4	≤ 0.5	12.7
1050	43.4 ± 6.5	9.8 ± 1.8	246.5 ± 79.3	≤ 1.0	23.1

3.3.2 EBSD Microstructures of Bonded Joints at Various Temperatures

The EBSD orientation maps of the joints bonded at different diffusion bonding temperatures are presented in Fig. 5. The micrographs on the left side (Fig. 5a, c, e and g) are the low magnification maps while the ones on the right side (Fig. 5b, d, f and h) are the zoom maps. The SS316L grains are relatively smaller than those of the CoCrFeMnNi grains. After bonding, there is still evidence of several twins in the SS316L microstructures. Table 4, presents the fraction of low-angle grain boundaries (LAGB) and high-angle grain boundaries (HAGB) in the SS316L and CoCrFeMnNi HEA microstructures for all the joints produced at different bonding temperatures. The fraction of LAGB and HAGB for SS316L microstructures produced after diffusion bonding at all the investigated temperatures were approximately 3% and 97%, respectively, this suggests that the SS316L grains

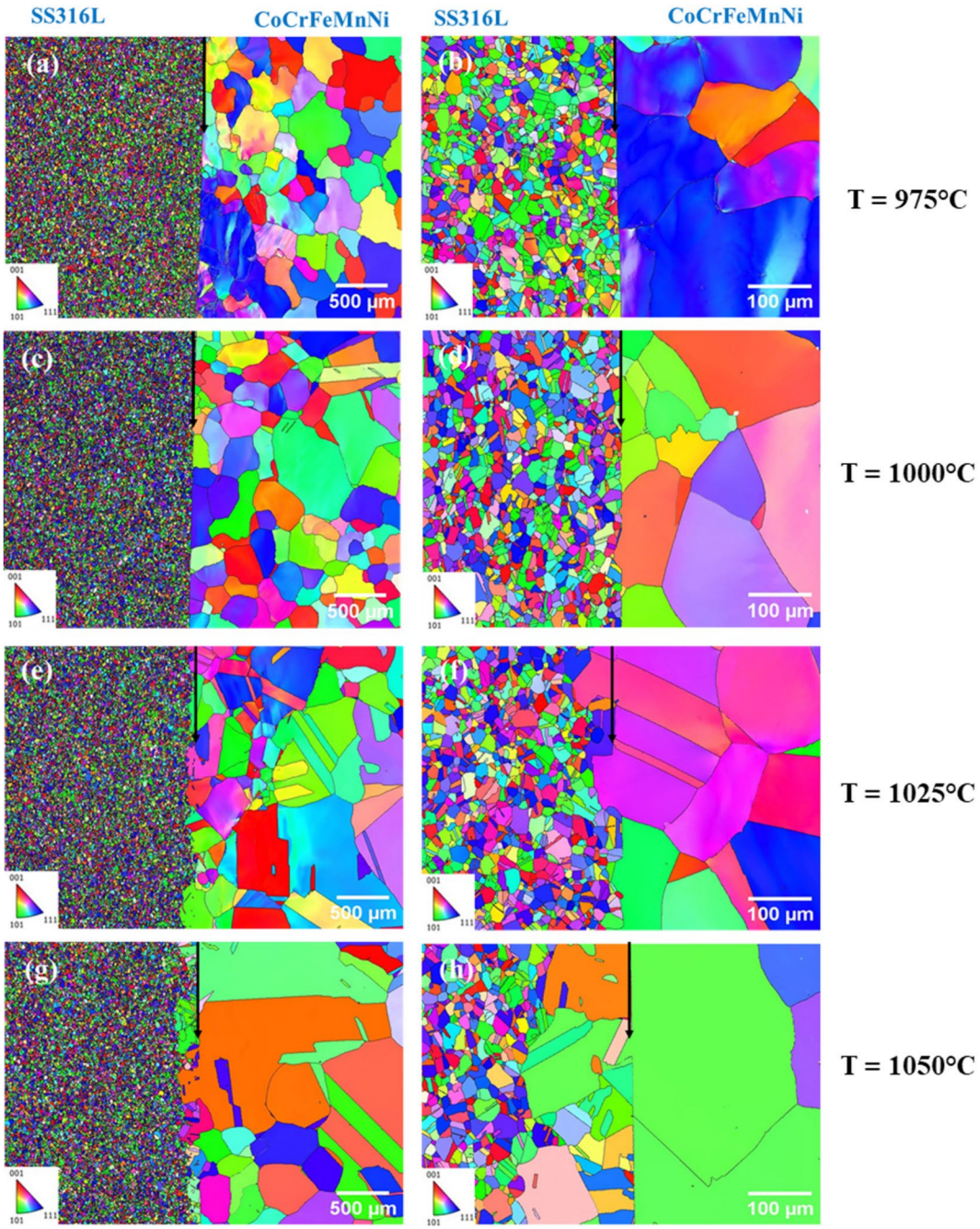

Fig. 5 EBSD orientation maps of SS316L-CoCrFeMnNi joints with the inverse pole figures (IPF) for the different temperature conditions (**a**) T = 975 °C, (**b**) T = 1000 °C, (**c**) T = 1025 °C, (**d**) T = 1050 °C (Black arrows in the microstructures indicate the locations of the bond interfaces)

Table 4 Summary of fraction of LAGB (2° − 15°) and HAGB (> 15°) in the microstructures shown in Fig. 5

Temperature (°C)	Microstructure	LAGB (%)	HAGB (%)
975	SS316L	3.0	97.0
	CoCrFeMnNi	31.9	68.1
1000	SS316L	3.2	96.8
	CoCrFeMnNi	5.9	94.1
1025	SS316L	3.0	97.0
	CoCrFeMnNi	7.9	92.1
1050	SS316L	2.9	97.1
	CoCrFeMnNi	3.0	97.0

were fully recrystallized due to the very high fraction of detected HAGB. At the low bonding temperature of 975 °C, the proportion of HAGB in the CoCrFeMnNi microstructure was 68.1% (see Table 4), which is lower and deviates from the values obtained at higher bonding temperatures. This implies that recrystallization of the HEA grains was not fully attained, which is in agreement with the presence of some distorted HEA grains near the bond interface reported above in Fig. 4a. For joints produced at bonding temperatures between 1000 and 1050 °C, the HEA grains were fully recrystallized as the proportion of HAGB was 94%–97%. At higher bonding temperatures of 1025 °C and above, grain growth across the bond interfaces occurred as observed in Figs. 5e– h. The bond interface lines became less visible, which can be attributed to the growth of the SS316L grains by epitaxy with those of the HEAs. The phase maps within the diffusion zone and across the microstructures observed for the joints produced at various temperatures presented a single FCC phase. A secondary or detrimental intermetallic phase was not observed despite variations in the bonding temperature.

3.4 EDS Line Analyses across the Bond Interface of Bonded Samples

3.4.1 Chemical Gradient across the Bond Interfaces

The EDS line profiles across the bond interfaces of the SS316L-CoCrFeMnNi joints at different bonding temperatures are shown in Fig. 6a – d illustrating the concentration gradient of diffusing elements with respect to positions from the interfaces. The constituents of CoCrFeMnNi HEA are in equiatomic ratio (20% at.) while SS316L majorly contains Fe, Cr, and Ni in atomic concentrations of about 68.5%, 18% and 9.5%, respectively (see Table 1). Using the bond interface as a reference, two interdiffusion zones I and II were defined, which are the mixing area of the diffused elements. Zone I is the diffusion zone of the SS316L side while zone II is the one on the CoCrFeMnNi side. The endpoints of the diffusion zones I and II were determined based on the interval between the bond interface and the points where the elements attain compositional stability on the EDS line scan data at the SS316L and HEA side respectively. The highest diffusion width at zone I and II was taken and the sum of these values is the entire diffusion width for each case.

From all the compositional line profiles, the Fe atom diffused from the SS316L across the bond interface towards the CoCrFeMnNi-HEA while Co, Ni, and Mn elements diffused across the interface towards the SS316L alloy. The diffusion of the Cr atom was not very obvious due to the similar concentration of this atom in the two base alloys. For bonding conducted at a temperature of 975 °C (Fig. 6a), the entire diffusion width was 6.8 µm with zone I and zone II having widths of 2.9 µm and 3.9 µm, respectively. As the bonding temperature was increased to 1000 °C, the total diffusion width also increased to 10.5 µm with zone I and zone II having diffusion widths of 5 µm and 5.5 µm, respectively. Further, a rise in the bonding temperature to 1025 °C and 1050 °C led to higher total diffusion widths of 14 µm and 17.5 µm, respectively. For all cases, the diffusion width at zone II was larger than that of zone I. Figure 7 shows the evolution of the diffusion widths at zones I, II, and I + II with respect to the reciprocal of bonding temperatures. The total diffusion width increases drastically over the temperature range as a change of 75 °C (from 975 to 1050 °C) triples the width of the diffusion zone. This may be explained by the fact that the diffusion is highly temperature-sensitive and follows the Arrhenius law. However, a slowdown in the increase of the diffusion width on the SS316L side (zone I) can be observed after the bonding temperature of 1025 °C and this will be discussed later.

3.4.2 Diffusion Coefficient and Activation Energy of Major Constituent Elements

The diffusion coefficient, D, of major constituent elements was determined analytically using Fick's second law of diffusion. The chemical composition line distribution in Fig. 6 provided information on the concentration and distance from the bond interface which was used to calculate the diffusion coefficient.

The values of the diffusion coefficients obtained in the SS316L side (zone I) and the CoCrFeMnNi side (zone II) at various bonding temperatures are presented in Table 5. The evolution of each diffusion coefficient with temperature is different in zone I compared to zone II, and this is for all the chemical elements. In zone I, it is observed that whatever the element, the diffusion coefficient increased with the temperature until 1025 °C and then decreased at 1050 °C. Conversely, in zone II, the diffusion coefficient continuously increases for all temperatures. The increase in the values of the diffusion coefficient is coherent with the increase of the diffusion width for the two zones for 975 °C,

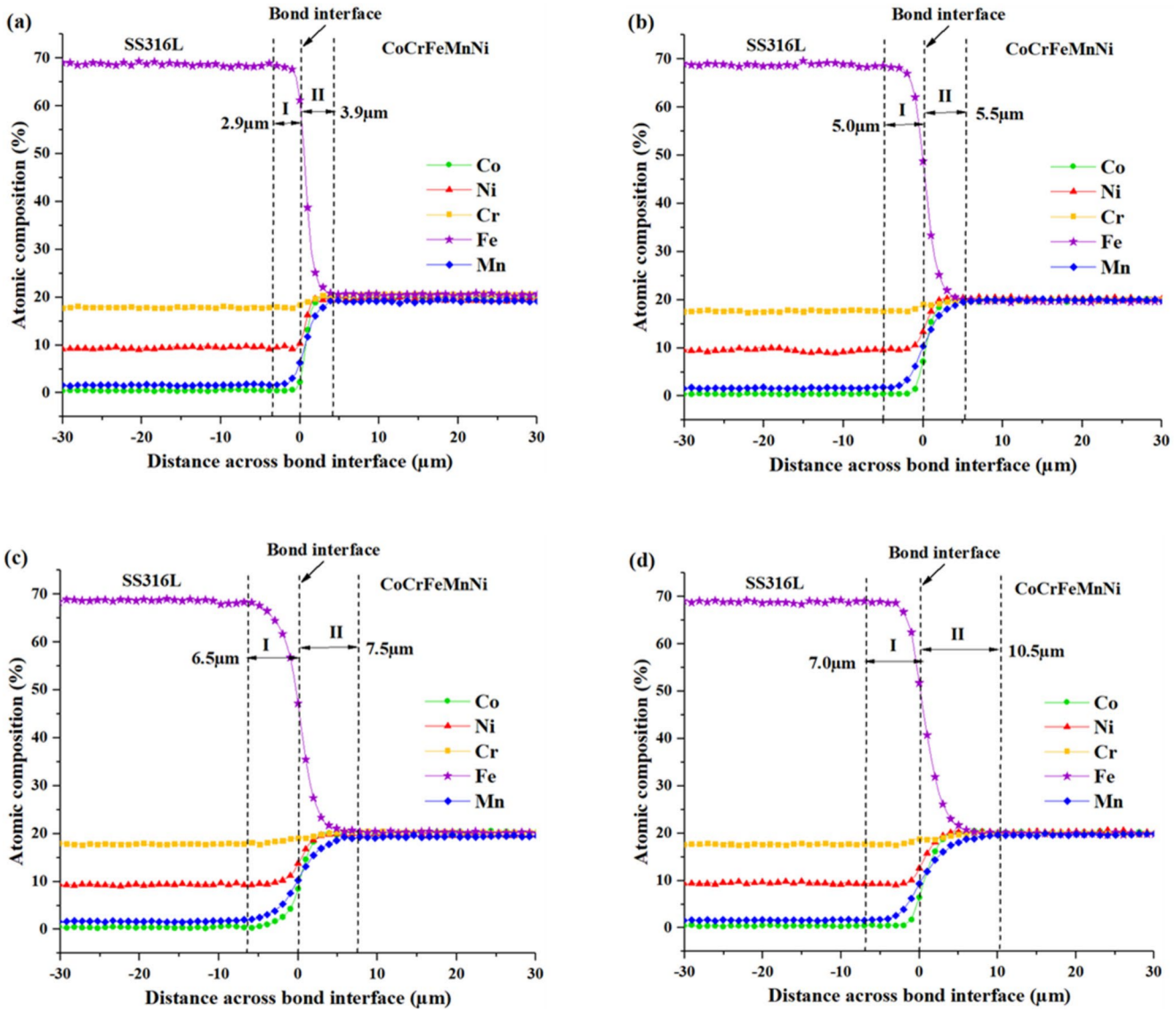

Fig. 6 Chemical gradients across the bond interfaces as determined by EDS analyses for SS316L-CoCrFeMnNi joints bonded at, (**a**) 975 °C, (**b**) 1000 °C, (**c**) 1025 °C, (**d**) 1050 °C

1000 °C, and 1025 °C. At 1050 °C, the increase in the diffusion width at zone I is not significant (Figs. 6 and 7) which is also correlated to the decrease of all the diffusion coefficients on the SS316L side. This trend might be attributed to the change in diffusional mechanisms due to the presence of porosity and grains of larger size in the diffusion zone. To go further in the analysis of the diffusion coefficient in zone II, Table 5 reveals that the fastest diffusing element is Mn, which was immediately followed by Fe, while the least diffusing atoms are Ni and Co. The computation of diffusion coefficients of the Cr atom would likely have a high percentage error because the atomic concentrations of this element in SS316L and CoCrFeMnNi HEA are very close. It can be noted that our experimental results are quite in agreement with other previous results for the chemical sequence: $D_{Mn} > D_{Fe} > D_{Co} \geq D_{Ni}$ [53, 54, 55].

The evolution of the diffusion coefficients with respect to the temperature was modelled using the Arrhenius equation given by:

$$D = D_o \exp(-\frac{Q}{RT}) \quad (2)$$

where Q is the activation energy of diffusion, D_o is the pre-exponential factor (m^2/s), T is the bonding temperature (K), and R is the ideal gas constant (8.314 J/mol.K). The Arrhenius law stays valid as long as the effective diffusional mechanisms do not change when temperature increases. It does not consider the evolution of effective diffusion

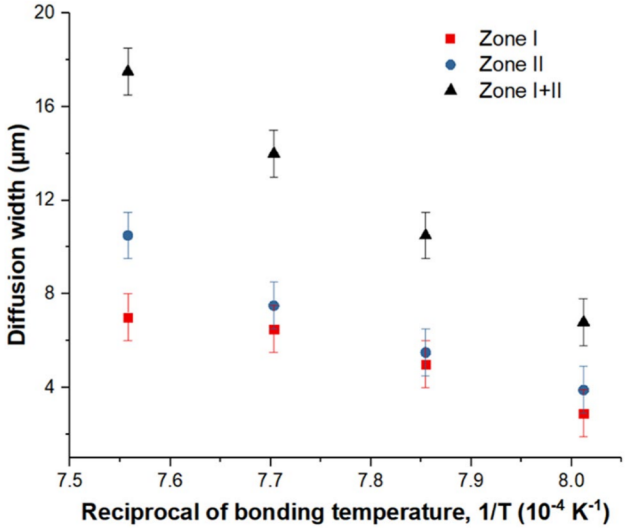

Fig. 7 Evolution of the diffusion widths of zones I, II and I+II with reciprocal of bonding temperature

Table 5 Diffusion coefficients, *D* of major elements at zone I (SS316L side) and zone II (CoCrFeMnNi side) under various bonding temperatures for 60 min (Diffusion coefficients of atoms moving across the bond interface into new materials are highlighted). The error bar is about ± 10%

Bonding temperatures (°C)	Diffusion coefficients (x 10^{-15} m^2/s)	D_{Co}	D_{Ni}	D_{Fe}	D_{Mn}
975	Zone I	**<0.001**	**<0.001**	0.02	**0.10**
	Zone II	0.11	0.12	**0.15**	0.30
1000	Zone I	**0.15**	**0.30**	0.30	**0.55**
	Zone II	0.15	0.11	**0.22**	0.45
1025	Zone I	**0.50**	**0.50**	0.80	**1.20**
	Zone II	0.20	0.20	**0.40**	0.75
1050	Zone I	**0.15**	**0.14**	0.30	**0.70**
	Zone II	0.35	0.40	**0.70**	1.10

coefficients due to the activation of other mechanisms such as change in grain size, creation of porosity, or precipitation. Especially, the effect of grain sizes on diffusion coefficients is well-known as grain boundaries act as preferential diffusional paths, meaning that coarse grains lead to smaller effective diffusion coefficients. For such reason, the identification of the parameters of the equations was omitted for the highest temperature investigated in this work, i.e., 1050 °C. For each zone II, the Arrhenius model was identified for each element by linearizing Eq. 2 with the natural logarithm function.

Figure 8 compares the evolution of the experimental diffusion coefficients identified for each element in Zone I (Fig. 8a) and Zone II (Fig. 8b). In zone II, the Arrhenius law is also plotted. However, Fig. 8a demonstrates that diffusion can not be modelled by an Arrhenius law on the whole range of temperature studied here. On the other side, in zone II, a very good correlation with the Arrhenius law was observed, with a score metric R^2 above 0.8 for each element. The values of the identified parameters such as the activation energy, the pre-exponential factor and the R^2 score are summarized in Table 6. From a microstructural point of view, the activation energy Q corresponds to the energy needed to jump between two atomic positions, to be compared to the energy provided to the atom by the temperature. On the other side, the pre-exponential factor D_o is closely linked with the lattice parameter and frequency of vibration of the diffusing atom. An increase in Q leads to a decrease in the diffusion coefficient, whereas an increase in D_o leads to an increase in the diffusion coefficient. From the trend observed in Table 6, the sequence for Q and D_o from the lowest to highest at the CoCrFeMnNi side is: Co < Ni < Mn < Fe.

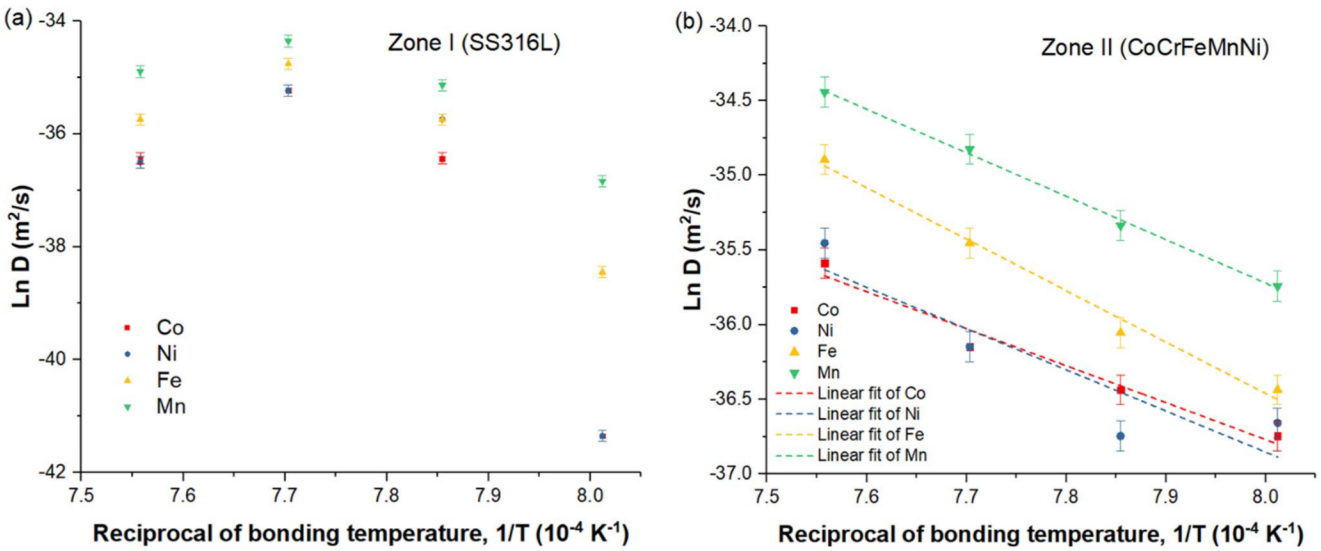

Fig. 8 Evolution of the diffusion coefficients, *ln(D)*, with respect to the reciprocal of the temperature, *1/T*, at (**a**) zone I, and (**b**) zone II (For zone II, linear fits according to Arrhenius law is plotted for each chemical species)

Table 6 Parameters of the kinetics diffusion of Co, Ni, Fe and Mn using the arrhenius law within CoCrFeMnNi HEA - zone II

Element	Present study			Vaidya et al. [56]		Tsai et al. [53]	
	Q (kJ/mol)	D_o (m^2/s)	R^2	Q* (kJ/mol)	D_o* (m^2/s)	Q* (kJ/mol)	D_o* (m^2/s)
Co	205.79	4.32×10^{-8}	0.9674	270±22	1.6×10^{-5}	306.9	9.26×10^{-4}
Ni	229.32	3.83×10^{-7}	0.8270	304±9	6.2×10^{-4}	317.5	19.7×10^{-4}
Fe	286. 00	1.33×10^{-4}	0.9891	309±11	1.3×10^{-3}	309.6	15.1×10^{-4}
Mn	241.95	4.01×10^{-6}	0.9972	272±13	1.6×10^{-4}	288.4	5.01×10^{-4}

Q is the activation energy, D_o is the pre-exponential factor while Q* and D_o* are values obtained from previous studies

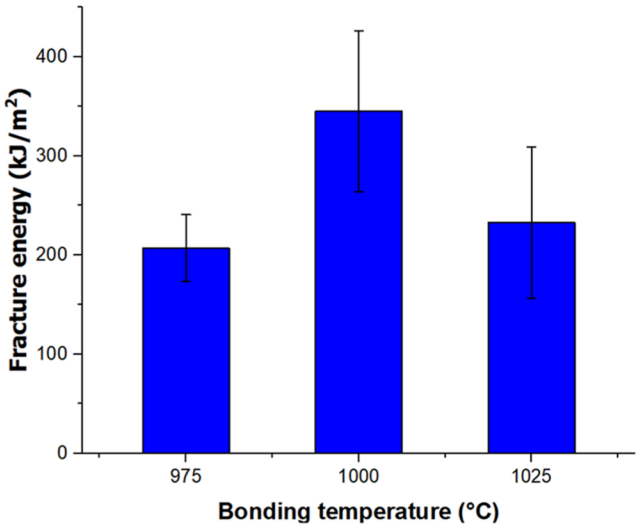

Fig. 9 Chart showing fracture energy required to rupture samples bonded at various temperatures (Three shear tests were conducted for each bonding condition and an average of these three readings was considered for interpreting the results)

Figure 8b shows that in zone II, where elements diffused within CoCrFeMnNi HEA, the evolution of the diffusion coefficients D with temperature are well fitted by the Arrhenius law. This means that in this zone, and for this temperature range, the same diffusional mechanisms occur, whatever the species or the temperature. Figure 8a shows that in zone I, above 1025 °C, the evolution of the diffusion coefficients for all the species deviates from Arrhenius law. This certainly means that other diffusional mechanisms operate at these temperatures.

Experimental Arrhenius law parameters for CoCrFeMnNi HEA are summarized in Table 6. For the sake of comparison, values of the parameters found by Vaidya et al. [56] and Tsai et al. [53] on the HEA material are also indicated. Some discrepancies can be found, which can be attributed to the fact that Vaidya et al. used very low concentrations of diffusing elements. Indeed, it is well-known that the D_o factors observed in these trace conditions are always higher. However, one can observe that Q values are close for the two studies and that the same chemical sequence exists for D_o: $D_{oFe} > D_{oMn} > D_{oNi} > D_{oCo}$. It could be mentioned that in the work of Tsai et al., non-equiatomic $CoCrFeMn_{0.5}Ni$ HEA with a grain size of approximately 0.5–1 mm was used, which justified the higher values of the activation energy.

3.5 Assessment of the Fracture Energy Based on Shear Tests

Shear tests were conducted for bonded samples produced at the three different bonding temperatures namely: 975 °C, 1000 °C and 1025 °C. Three tests were conducted each for the three different bonding conditions. The mechanical responses of all the diffusion-bonded joints were assessed based on the fracture energy, G_f (defined in Eq. 1) obtained from the shear test results (Fig. 9). The fracture energy is a measure of the fracture toughness hence, the higher the fracture energy, the higher the fracture toughness [57]. The lowest fracture energy was observed with the sample bonded at 975 °C (0.78 T_m) which is 207.2±33.6 kJ/m^2. This implies that the joint produced at 975 °C will have the lowest fracture toughness. SS316L-CoCrFeMnNi joint produced at a bonding temperature of 1000 °C (0.79 T_m) had the highest fracture energy of 345.1±81.1 kJ/m^2 and by extension will also have the highest fracture toughness. Diffusion bonding of SS316L and CoCrFeMnNi HEA at a temperature of 1025 °C (0.81 T_m) had an intermediate fracture energy of 233.0±76.4 kJ/m^2.

3.6 Fractography of the SS316L-CoCrFeMnNi Ruptured Surfaces

The SS316L-CoCrFeMnNi ruptured surfaces were examined to understand the fracture mode and identify the fracture location. The fractographs as observed under the SEM are presented in Fig. 10. revealing the topography of the fractured surfaces. Figure 10 (a, c & e) displayed the SS316L side while Fig. 10 (b, d & f) showed the HEA side. For the sample joined at a bonding temperature of 975 °C, fine shallow dimples were observed as shown in Fig. 10 (a – b). The sample bonded at a temperature of 1000 °C (Fig. 10 (c – d)) revealed coarse dimples and some cavities, while the sample joined at a bonding temperature of 1025 °C presented coarser dimples and cavities as shown in Fig. 10 (e – f). The presence of several dimples as observed in the fractographs implies that all the bonded samples failed in

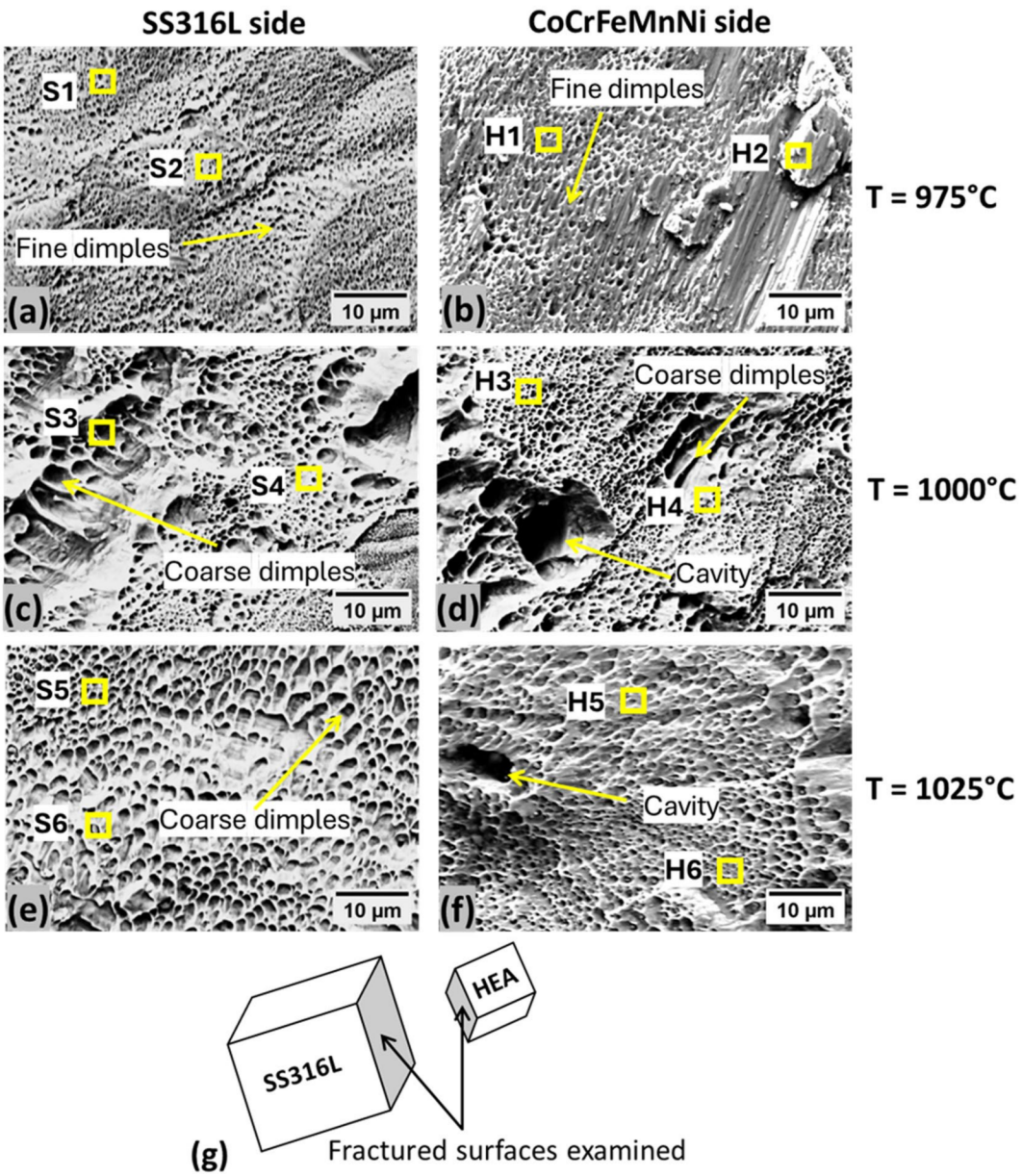

Fig. 10 Fractographs of the SS316L-CoCrFeMnNi ruptured surfaces showing various features for joints produced at bonding temperatures of (**a**, **b**) 975 °C, (**c**, **d**) 1000 °C, (**e**, **f**) 1025 °C (**g**) SS316L and HEA fractured surfaces examined

ductile fracture mode. However, it is clear from Fig. 10 that as the bonding temperature increased, the size of the dimples became larger. The chemical composition of some locations on the fractographs taken with the SEM-EDS are presented in Table 7. The locations S1 – S6 are all on the SS316L side while locations H1 – H6 are on the CoCrFeMnNi HEA side. By comparing the chemical composition in Table 7 with that of the EDS chemical line data across the bond interfaces for the three bonding conditions earlier obtained, the fracture location was identified. The results revealed that at the different bonding temperatures of 975 °C, 1000 °C and 1025 °C, the failure occurred majorly at zone II which is the CoCrFeMnNi side.

3.7 Phase Analyses of the Fractured Surfaces

The XRD patterns of the fractured bonded samples produced at temperatures of 975°C, 1000°C, and 1025°C are presented in Fig. 11. Since the bonded samples were fractured into two distinct surfaces, phase analysis was performed on the fractured surfaces on the SS316L side (Fig. 11a) as well as on the CoCrFeMnNi side (Fig. 11b). Both surfaces displayed peaks majorly at {111}, {200}, and {220} planes, which is a

Table 7 Chemical composition (at%) at the marked locations in Fig. 10 (Zone I is at SS316L side and zone II is at CoCrFeMnNi side)

Bonding temp. (°C)	Position	Co	Ni	Cr	Fe	Mn	Fracture location
975	S1	6.19	12.06	18.94	53.50	8.24	Zone II
	S2	7.30	12.61	19.06	51.09	8.90	Zone II
	H1	13.69	15.14	19.89	37.56	12.71	Zone II
	H2	7.44	12.29	19.08	51.14	8.89	Zone II
1000	S3	6.48	11.83	19.12	53.08	8.35	Interface
	S4	10.88	14.32	19.28	44.42	10.25	Zone II
	H3	13.31	15.26	19.48	38.02	12.99	Zone II
	H4	11.93	14.64	19.50	41.32	11.77	Zone II
1025	S5	8.16	12.93	18.96	49.42	9.55	Interface
	S6	8.89	13.30	19.71	46.72	10.45	Interface
	H5	14.37	15.84	19.19	37.12	12.41	Zone II
	H6	13.79	14.93	19.48	38.10	12.48	Zone II

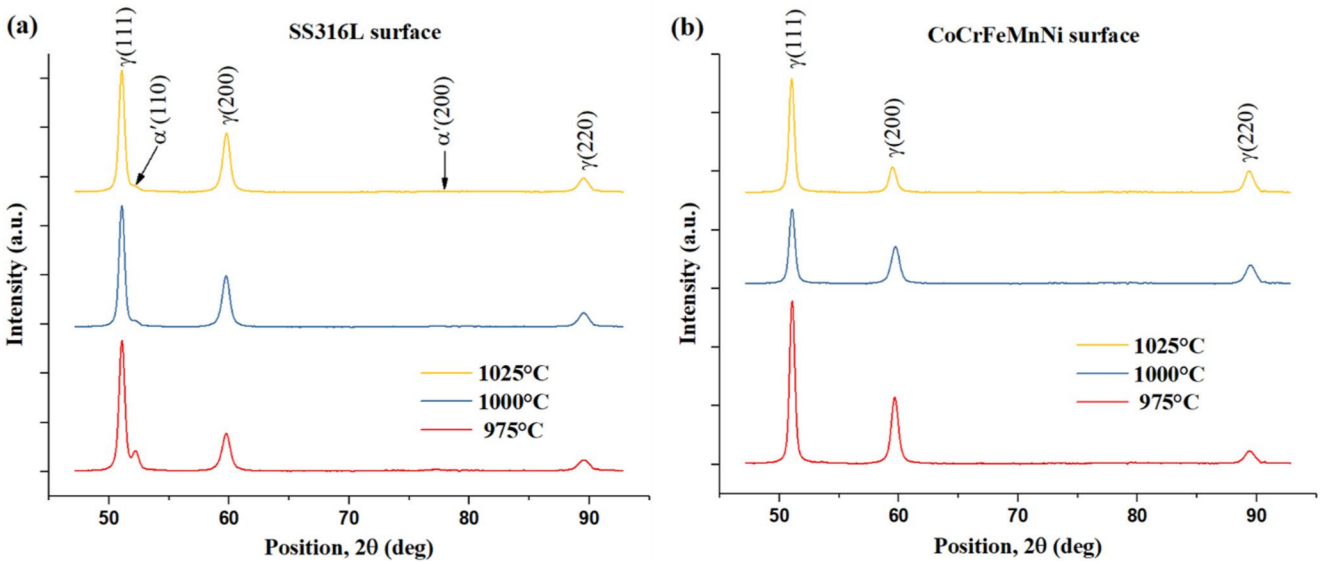

Fig. 11 XRD patterns of the fractured SS316L-CoCrFeMnNi joints bonded at different temperatures, (**a**) SS316L fractured surfaces (**b**) CoCrFeMnNi fractured surfaces

characteristic of FCC crystal, for similar diffraction angles, suggesting comparable values of the lattice parameters. This trend was similarly observed in the base samples in Fig. 3. At the SS316L side fractured surfaces (Fig. 11a), additional peaks from the {110} and {200} planes appeared for the diffraction angles 2θ ~ 52° and 2θ ~ 78°, respectively. These are body-centred tetragonal (BCT) martensitic peaks, which were strain-induced by large plastic deformation during the fracture process. A small peak of α' martensite was similarly observed when a solution-treated SS316L was fractured after tensile loading [58]. SS316L is a material with low stacking fault energy and high Md (Md: the maximum temperature at which the deformation-induced martensitic transformation can take place) value, which makes it susceptible to the strain-induced transformation of the austenitic to martensitic phase when deformed. It is important to state that the XRD patterns did not reveal any carbide-based intermetallic peaks for all the fractured samples that were joined at various bonding temperatures.

4 Discussion

A close examination of all the samples bonded at various temperatures confirmed that no major defects like cracks were formed. On further examination of the microstructural evolution, samples produced at bonding temperatures of 975 °C, and 1000 °C had better joints than those produced at bonding temperatures of 1025 °C and 1050 °C. These samples had better microstructural continuity in terms of the fraction of interfacial pores and no SS316L grain coarsening could be detected near the bond interfaces. Under these investigated conditions, the diffusion bonding at 1000 °C was found to be the best based on all the microstructural examinations. In addition to the good qualities earlier stated, the HEA grains were not distorted as observed at the lower bonding temperature due to full recrystallisation of the grains in the entire microstructure. Diffusion bonding conducted at bonding temperatures of 1025 °C and 1050 °C, which is equivalent to 0.81 T_m and 0.83 T_m, respectively,

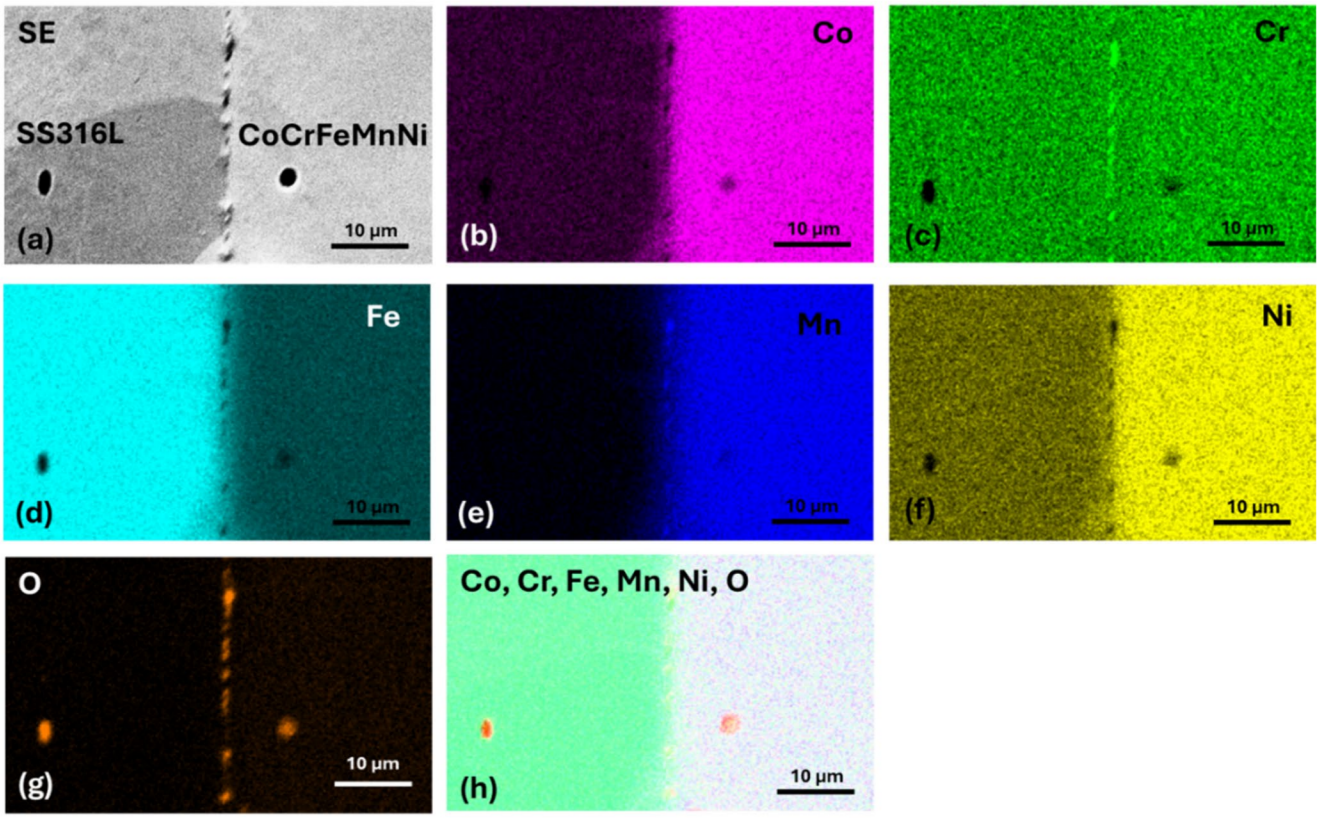

Fig. 12 Chemical maps of the microstructure of SS316L-CoCrFeMnNi joint diffusion welded at 1050 °C (**a**) Secondary electron image (**b** – **g**) Chemical maps of each constituent element (**h**) Chemical map containing all major constituent elements

led to grain growth of the SS316L near the bond interface as well as an increase in the interfacial porosity in terms of size and density as already observed.

The grain growth of the SS316L has been reported to be rapid at temperatures above 1038 °C under various investigations [58, 59, 60]. The higher interfacial porosity observed at increased bonding temperature could be attributed to the Kirkendall effect as a result of the inequalities of diffusion rates of atoms. At varying temperatures, a shift in the diffusion path mechanism can occur. As the rate of diffusion increases, excessive grain boundary migration and diffusion along defects are triggered. Since there is a difference in the diffusivity of the atoms between the two materials, this leads to an accumulation of vacancies that coalesce into micropores in the vicinity of the bond interface. The SS316L grain growth at the interface could cause stress or misalignment of the grain boundaries, which can create voids. The unequal diffusion flux within the SS316L-CoCrFeMnNi system at the high bonding temperature of 1050 °C is evident from the segregation of Cr and Mn atoms around the interfacial voids as shown in Fig. 12. The diffusion coefficients of elements presented in Table 5 also confirmed that Mn has the highest value of diffusion coefficient, which will make it migrate rapidly towards short circuit channels. It is important to note that despite the vacuum environment in which the diffusion bonding was conducted, there might be minor traces of oxygen in the system, which could interact with accumulated Cr and Mn atoms and form manganese spinel Cr_2MnO_4 at very high bonding temperatures. The spinel formation has been reported during high-temperature oxidation of chromium-manganese alloys at temperatures of 900 °C and 1000 °C [61, 62, 63].

The bond interfaces for all the bonded samples were characterised by the interdiffusion of elements, which eventually formed diffusion zones I and II. The back-scattered electron (BSE) images at high magnification, phase maps derived from EBSD maps, the EDS chemical analysis and the XRD patterns of the ruptured bonded samples revealed that the formed diffusion zones consisted of essentially the FCC phase. No intermetallic carbides or any other detrimental phase could be detected within the diffusion zones, which is in agreement with the study performed by Sun et al. [47]. It is also important to state that changing the bonding temperature did not cause any phase transformation to take place. For all the samples bonded at different temperatures, there was a similar trend in the type of elements that diffused across the bond interface. Fe diffused towards CoCrFeMnNi HEA while Mn, Cr, Co and Ni diffused towards the SS316L.

The diffusion of Cr is not very significant as its composition in CoCrFeMnNi HEA and SS316L are close. The EDS chemical line scan of all the bonded samples presented in Fig. 6 and the diffusion width versus bonding temperature plot (Fig. 7) revealed that the diffusion widths at zones I and II increased as the bonding temperature increased. The results shown in Fig. 6 also revealed that the diffusion width is larger in HEA than in the SS316L. This implies that diffusion is more effective in the HEA than in SS316L, which is in contradiction with the commonly accepted sluggish diffusion concept. The higher diffusion in the HEA may also be because the liquidus temperature of the HEA is lower than that of SS316L, and so the bonding temperature is closer to the liquidus temperature in HEA. The sluggish diffusion in high entropy alloys is still under debate. Studies asserting that sluggish diffusion exists in these materials [53, 64] explain this phenomenon by the fact that, due to the variety of surrounding atoms of each lattice site, there is a vacancy trapping effect of some low-energy sites. Choi et al. [64] found by simulation that the energy barrier for the migration of Mn atoms is generally smaller than those of Co and Ni, in such a way that Mn diffuses more than Co and Ni. From these studies, the evidence of sluggish diffusion is based on interdiffusion experiments and some simplification assumptions. Their results were successfully modelled by Paul et al. [65], using various diffusion kinetics theories, leading to obtaining self-diffusivities values. The conclusion of Tsai et al. [53] suggesting that sluggish diffusion exists in HEA alloy is mainly based on their result that Q/T_m is higher for HEA than for other alloys. Vaidya et al. [56, 66] critically discussed the conclusions made by Tsai et al. [53] when they experimentally studied element diffusion in equiatomic CoCrFeMnNi HEA using radioactive tracers. Their results do not support the existence of special sluggish diffusion in HEA. Among other considerations, Vaidya et al. mentioned the specific role of Mn that lowers melting temperature and has strong interaction with Ni increasing the average enthalpy of mixing of Ni, $|\Delta H^{Ni}_{avg}|$ value that lowers Ni diffusion. They proposed that the term "sluggish diffusion" may be restricted to the fact that configurational entropy drastically increases when more chemical elements are added. However, they underlined the fact that one has to take into account the nature of the chemical element added to the alloy. Furthermore, the work of Kuzca et al. [54] and Kottke et al. [67] do not agree with the existence of sluggish diffusion. Divinski et al. [68] critically reviewed the different experimental works. They also concluded that sluggish diffusion due to the existence of numerous chemical elements is not proven, whereas the importance of cross-correlations in the diffusion of different species in HEAs has to be taken into account.

The diffusion behaviour of the constituent elements can be understood based on the diffusion coefficients, activation energy and pre-exponential factors presented in Tables 5 and 6. The results confirmed that an incremental change in the bonding temperature caused an increase in the diffusion coefficient. This increase can be well described by an Arrhenius law in HEA (zone II), which would suggest that the same diffusional mechanism operates in the studied temperature range. At the SS316L side (zone I), the diffusion coefficient decreased at a bonding temperature of 1050 °C, which means that the Arrhenius law was not respected especially under this condition. A different diffusion mechanism might have prevailed at this condition largely due to the microstructural changes at the bond interface. It can be observed in Fig. 5(g – h) that the epitaxial grains grow from CoCrFeMnNi HEA towards the SS316L side. Another factor that can influence the change in diffusion mechanism is the presence of several twins as revealed in Fig. 5. Twins have special grain boundaries which can either promote or retard diffusion depending on the type.

A high diffusion coefficient is an indication of a fast diffusion rate while a high activation energy implies that the diffusion will be more difficult, i.e., requiring a greater energy to allow the atoms to move between lattice positions. The pre-exponential factor (D_o) also influences values of the diffusion coefficient [51, 69, 70, 71]. The fastest diffusing element is the Mn atom followed by the Fe atom and the slowest are the Ni and Co atoms, this trend has also been reported in previous studies [53, 56]. Bulk tracer diffusion in equiatomic CoCrFeMnNi HEA was conducted [56], and the activation energies, Q of Co, Cr, Fe and Mn obtained in the study were slightly higher than those reported in this study (see Table 6). Generally, the activation energy for bulk diffusion is expected to be higher in comparison to the activation energy for the grain boundary diffusion mechanism [72]. The values of the pre-exponential factor, D_o are also higher than those obtained in this study, which can be attributed to the very low concentrations of diffusing elements used in the previous study.

The fracture energy is an estimation of the minimum energy required to break the bond between SS316L and CoCrFeMnNi, and it is a more relevant parameter for assessing materials that fail in a more ductile manner. Since the fracture energy is a measure of the fracture toughness, the joint with the lowest fracture toughness is the one bonded at 975 °C (0.78 T_m). This joint had the lowest diffusion width and its microstructure was associated with some residual stress which must have negatively affected the bond formed. The joint produced at a bonding temperature of 1000 °C (0.79 T_m) had the highest fracture energy and by extension will also have the highest fracture toughness. In previous work, the fracture energy of equiatomic CoCrFeMnNi HEA

at room temperature was reported to be 250kJ/m^2 [21]. It is important to note that the test conditions and the rigidity of the machines used can influence the final values of fracture energy obtained. Diffusion bonding at a temperature of 1000 °C gave a combination of the highest fracture energy of 345kJ/m^2, a diffusion width of 10.5 µm, and the lowest interfacial pore size and density resulting in the best bond. When SS316L-CoCrFeMnNi joints were produced by spark plasma sintering diffusion bonding under a compressive pressure of 25 MPa for 60 min and at bonding temperatures of 900 °C, 950 °C and 1000 °C, the best joint was obtained at a bonding temperature of 1000 °C because it had sufficient diffusion, least voids at the bond interface and the highest tensile strength [47]. Although diffusion bonding at 1025 °C (0.81 T_m) had a higher diffusion width of 14 µm, this did not translate into the strongest joint. The joint was compromised due to the larger pore size, the lower bonding rate and the coarsening of SS316L grains taking place near the bond interfaces can account for the softening in this region. Results reported by Sun et al. [47] are in agreement with this study which also recommended 1000 °C for 1 h as the optimum bonding temperature for conducting conventional diffusion bonding between equiatomic CoCrFeMnNi and SS316L. Most authors recommended that diffusion bonding of many metals and alloys is best carried out by applying temperatures up to 60%–80% of the melting temperature of the base material with the lowest melting point [45, 51]. Hence, diffusion bonding at temperatures above 0.8 T_m did not produce the optimum results. The bonding temperature between equiatomic CoCrFeMnNi and SS316L is a critical parameter influencing the microstructural characteristics, diffusion kinetics and joint integrity. Hence, adequate attention should be ensured to set the most suitable value.

5 Conclusions

Diffusion bonding was successfully conducted between equiatomic CoCrFeMnNi HEA and 316 L stainless steel for 1 h within a temperature range between 975 °C and 1050 °C corresponding to 0.78 to 0.83T_m of the melting temperature of CoCrFeMnNi HEA. The microstructures, and diffusion mechanisms of the bonded samples were examined using a Scanning Electron Microscope equipped with an Energy Dispersive Spectrometer (SEM-EDS), Electron Back-Scattered Diffraction (EBSD) and X-ray Diffraction (XRD) analyses. Diffusion coefficients of constituent elements were analytically determined based on the Fick's second law of diffusion. The mechanical responses of bonded samples were assessed based on the fracture energy obtained from the shear test results. Finally, the fractured bonded samples were examined with the X-ray diffractometer. The findings obtained from this study are summarised as follows:

i) The interdiffusion of elements across the bond interface led to the formation of diffusion zones which consisted majorly of FCC-single phase. The variation in the bonding temperature did not cause any phase transformation, formation of intermetallic carbides or other detrimental phases.
ii) An incremental change in the bonding temperature led to a widening of the diffusion zones, and an increase in the diffusion widths.
iii) Microstructural changes in the bonded samples become prominent when joints are produced at a bonding temperature of 1025 °C and above.
iv) Diffusion bonding of SS316L-CoCrFeMnNi at a temperature of 1000 °C (0.79 T_m) produced a joint with sufficient diffusion, little interfacial pores and the highest fracture energy hence diffusion bonding at this condition is highly recommended. Samples bonded at a temperature above this optimum temperature do not improve the quality of the joint.

One single factor does not define the quality of the bond but a combination of several factors. The quality of the joint was found to be dependent upon the absence of interfacial porosities and brittle intermetallic phases at the diffusion zones. A uniform FCC crystalline structure is also favourable, as well as a large diffusion zone allowing good junction and smooth changes in lattice parameters leading to minimal lattice distortion and internal stresses. In this context, one important point is the optimization of the chemical composition of the alloys, and thermodynamic calculations to evaluate the possibility of formation of intermetallics with respect to temperature. Other important points include optimisation of the microstructures at the boundaries, recrystallization, epitaxial growth across the joint, and twinning. For that purpose, one must pay attention to parameters such as the initial grain sizes, the density of initial defects and the initial crystalline texture of the base materials. Other general parameters should be explored such as the use of interlayer materials between the HEA and SS316L, the bonding time, temperature, pressure exerted during bonding and the bonding atmosphere.

Acknowledgements This research was financially supported by the Petroleum Technology Development Fund (PTDF), Nigeria. The authors acknowledge Yudong Zhang, Jean-Sébastien Lecomte and the staff of the experimental facilities (MicroMat) from LEM3 (Université de Lorraine - CNRS UMR 7239), Marc Wary (Ecole Nationale Superieure Arts et Metiers, Metz) and Marie Noëlle Avettand Fenoël (Univ. Lille, CNRS, INRAE, Centrale Lille, UMR 8207 - UMET, Lille-France) for their technical support.

Declarations

Competing interests The authors declare that they have no known competing financial interests or personal relationships that could have appeared to influence the work reported in this paper.

References

1. B. Cantor, I.T.H. Chang, P. Knight, A.J.B. Vincent, Microstructural development in equiatomic multicomponent alloys. Mater. Sci. Eng. A **375–377**, 213–218 (2004). https://doi.org/10.1016/j.msea.2003.10.257
2. J.-W. Yeh et al., Nanostructured high-entropy alloys with multiple principal elements: novel alloy design concepts and outcomes. Adv. Eng. Mater. **6**(5), 299–303 (2004). https://doi.org/10.1002/adem.200300567
3. M.C. Gao, J.-W. Yeh, P.K. Liaw, Y. Zhang (eds.), *High-Entropy Alloys - Fundamentals and Applications* (Springer, Cham, 2016). https://doi.org/10.1007/978-3-319-27013-5
4. B.S. Murty, J.W. Yeh, S. Ranganathan, P.P. Bhattacharjee, *High-Entropy Alloys*, 2nd edn. (Elsevier, Amsterdam, 2019)
5. T.S. Srivatsan, M. Gupta (eds.), *High Entropy Alloys: Innovations, Advances, and Applications* (CRC, Boca Raton, 2020)
6. Y.L. Chou, Y.C. Wang, J.W. Yeh, H.C. Shih, Pitting corrosion of the high-entropy alloy $Co_{1.5}CrFeNi_{1.5}Ti_{0.5}Mo_{0.1}$ in chloride-containing sulphate solutions. Corros. Sci. **52**(10), 3481–3491 (2010). https://doi.org/10.1016/j.corsci.2010.06.025
7. M.-H. Chuang, M.-H. Tsai, W.-R. Wang, S.-J. Lin, J.-W. Yeh, Microstructure and wear behavior of $Al_xCo_{1.5}CrFeNi_{1.5}Ti_y$ high-entropy alloys. Acta Mater. **59**(16), 6308–6317 (2011). https://doi.org/10.1016/j.actamat.2011.06.041
8. R. Li, L. Guo, Y. Liu, Q. Xu, Q. Peng, Irradiation Resistance of CoCrCuFeNi High Entropy Alloy under Successive Bombardment. Acta Metall. Sin. (Engl. Lett.). **36**(9), 1482–1492 (2023). https://doi.org/10.1007/s40195-023-01577-w
9. O.N. Senkov, G.B. Wilks, J.M. Scott, D.B. Miracle, Mechanical properties of $Nb_{25}Mo_{25}Ta_{25}W_{25}$ and $V_{20}Nb_{20}Mo_{20}Ta_{20}W_{20}$ refractory high entropy alloys. Intermetallics. **19**(5), 698–706 (2011). https://doi.org/10.1016/j.intermet.2011.01.004
10. C.-J. Tong et al., Mechanical performance of the al X cocrcufeni high-entropy alloy system with multiprincipal elements. Metall. Mater. Trans. A **36**(5), 1263–1271 (2005). https://doi.org/10.1007/s11661-005-0218-9
11. M.-H. Tsai et al., Thermal stability and performance of NbSiTaTiZr high-entropy alloy barrier for copper metallization. J. Electrochem. Soc. **158**(11), H1161 (2011). https://doi.org/10.1149/2.056111jes
12. N.K. Adomako, G. Shin, N. Park, K. Park, J.H. Kim, Laser dissimilar welding of CoCrFeMnNi-high entropy alloy and duplex stainless steel. J. Mater. Sci. Technol. **85**, 95–105 (2021). https://doi.org/10.1016/j.jmst.2021.02.003
13. J.G. Lopes, J.P. Oliveira, A short review on welding and joining of high entropy alloys. Metals. **10**(2), 212 (2020). https://doi.org/10.3390/met10020212
14. H. Nam et al., Weldability of cast CoCrFeMnNi high-entropy alloys using various filler metals for cryogenic applications. J. Alloys Compd. **819**, 153278 (2020). https://doi.org/10.1016/j.jallcom.2019.153278
15. S.S. Huang, H.Q. Guan, Z.H. Zhong, M. Miyamoto, Q. Xu, Effect of he on the irradiation resistance of equiatomic CoCrFeMnNi high-entropy alloy. J. Nucl. Mater. **561**, 153525 (2022). https://doi.org/10.1016/j.jnucmat.2022.153525
16. H. Luo, Z. Li, A.M. Mingers, D. Raabe, Corrosion behavior of an equiatomic CoCrFeMnNi high-entropy alloy compared with 304 stainless steel in sulfuric acid solution. Corros. Sci. **134**, 131–139 (2018). https://doi.org/10.1016/j.corsci.2018.02.031
17. A. Rodriguez, J.H. Tylczak, M. Ziomek-Moroz, Corrosion behavior of CoCrFeMnNi high-entropy alloys (HEAs) under aqueous acidic conditions. ECS Trans. **77**(11), 741–752 (2017). https://doi.org/10.1149/07711.0741ecst
18. Q. Xu, H.Q. Guan, Z.H. Zhong, S.S. Huang, J.J. Zhao, Irradiation resistance mechanism of the CoCrFeMnNi equiatomic high-entropy alloy. Sci. Rep. **11**(1), 608 (2021). https://doi.org/10.1038/s41598-020-79775-0
19. Q. Xu, H.Q. Guan, S.S. Huang, Z.H. Zhong, H. Watanabe, M. Tokitani, Compositional stability in medium and high-entropy alloys of CoCrFeMnNi system under ion irradiation. J. Alloys Compd. **926**, 166697 (2022). https://doi.org/10.1016/j.jallcom.2022.166697
20. A. Gali, E.P. George, Tensile properties of high- and medium-entropy alloys. Intermetallics. **39**, 74–78 (2013). https://doi.org/10.1016/j.intermet.2013.03.018
21. B. Gludovatz, A. Hohenwarter, D. Catoor, E.H. Chang, E.P. George, R.O. Ritchie, A fracture-resistant high-entropy alloy for cryogenic applications. Science. **345**(6201), 1153–1158 (2014). https://doi.org/10.1126/science.1254581
22. F. Otto, A. Dlouhý, C. Somsen, H. Bei, G. Eggeler, E.P. George, The influences of temperature and microstructure on the tensile properties of a CoCrFeMnNi high-entropy alloy. Acta Mater. **61**(15), 5743–5755 (2013). https://doi.org/10.1016/j.actamat.2013.06.018
23. F.C. Garcia Filho, S.N. Monteiro, Welding joints in high entropy alloys: a short-review on recent trends. Materials. **13**(6), 1411 (2020). https://doi.org/10.3390/ma13061411
24. M. John et al., Welding techniques for high entropy alloys: processes, properties, characterization, and challenges. Materials. **15**, 2273 (2022). https://doi.org/10.3390/ma15062273
25. J. Li, X. Meng, L. Wan, Y. Huang, Welding of high entropy alloys: progresses, challenges and perspectives. J. Manuf. Process. **68**, 293–331 (2021). https://doi.org/10.1016/j.jmapro.2021.05.042
26. M. Rhode, T. Richter, D. Schroepfer, A.M. Manzoni, M. Schneider, G. Laplanche, Welding of high-entropy alloys and compositionally complex alloys—an overview. Weld World. **65**(8), 1645–1659 (2021). https://doi.org/10.1007/s40194-021-01110-6
27. T. Sonar, M. Ivanov, E. Trofimov, A. Tingaev, I. Suleymanova, A comprehensive review on fusion welding of high entropy alloys–Processing, microstructural evolution and mechanical properties of joints. Int. J. Lightweight Mater. Manuf. **7**(1), 122–183 (2024). https://doi.org/10.1016/j.ijlmm.2023.06.003
28. M.-G. Jo et al., Microstructure and mechanical properties of friction stir welded and laser welded high entropy alloy CrMnFeCoNi. Met. Mater. Int. **24**(1), 73–83 (2018). https://doi.org/10.1007/s12540-017-7248-x
29. N. Kashaev, V. Ventzke, N. Stepanov, D. Shaysultanov, V. Sanin, S. Zherebtsov, Laser beam welding of a CoCrFeNiMn-type high entropy alloy produced by self-propagating high-temperature synthesis. Intermetallics. **96**, 63–71 (2018). https://doi.org/10.1016/j.intermet.2018.02.014
30. H. Nam, C. Park, J. Moon, Y. Na, H. Kim, N. Kang, Laser weldability of cast and rolled high-entropy alloys for cryogenic applications. Mater. Sci. Eng. A **742**, 224–230 (2019). https://doi.org/10.1016/j.msea.2018.11.009
31. J.P. Oliveira et al., Gas tungsten Arc welding of as-rolled CrMnFeCoNi high entropy alloy. Mater. Design. **189**, 108505 (2020). https://doi.org/10.1016/j.matdes.2020.108505
32. Z. Wu, S.A. David, Z. Feng, H. Bei, Weldability of a high entropy CrMnFeCoNi alloy. Scripta Mater. **124**, 81–85 (2016). https://doi.org/10.1016/j.scriptamat.2016.06.046

33. Z. Wu, S.A. David, D.N. Leonard, Z. Feng, H. Bei, Microstructures and mechanical properties of a welded CoCrFeMnNi high-entropy alloy. Sci. Technol. Weld. Join. **23**(7), 585–595 (2018). https://doi.org/10.1080/13621718.2018.1430114
34. J.-Y. Lin, Z.-H. Lai, T. Otsuki, H.-W. Yen, S. Nambu,.Gradient microstructure and interfacial strength of CoCrFeMnNi high-entropy alloy in solid-state ultrasonic welding. Mater. Sci. Eng. A **825**, 141885 (2021). https://doi.org/10.1016/j.msea.2021.141885
35. S. Park, H. Nam, J. Park, Y. Na, H. Kim, N. Kang, Superior-tensile property of CoCrFeMnNi alloys achieved using friction-stir welding for cryogenic applications. Mater. Sci. Eng. A **788**, 139547 (2020). https://doi.org/10.1016/j.msea.2020.139547
36. N.K. Adomako, J.H. Kim, Microstructure and mechanical properties of dissimilar laser lap joint between CoCrFeMnNi-high entropy alloy and duplex stainless steel. Mater. Lett. **288**, 129354 (2021). https://doi.org/10.1016/j.matlet.2021.129354
37. H. Nam, S. Park, E.-J. Chun, H. Kim, Y. Na, N. Kang, Laser dissimilar weldability of cast and rolled CoCrFeMnNi high-entropy alloys for cryogenic applications. Sci. Technol. Weld. Join. **25**(2), 127–134 (2020). https://doi.org/10.1080/13621718.2019.1644471
38. J.P. Oliveira et al., Dissimilar laser welding of a CoCrFeMnNi high entropy alloy to 316 stainless steel. Scripta Mater. **206**, 114219 (2022). https://doi.org/10.1016/j.scriptamat.2021.114219
39. J. Xin et al., Dissimilar laser welding of CrMnFeCoNi high entropy alloy and 316LN stainless steel for cryogenic application. J. Mater. Sci. Technol. **163**, 158–167 (2023). https://doi.org/10.1016/j.jmst.2023.04.030
40. M. Rhode, K. Erxleben, T. Richter, D. Schroepfer, T. Mente, T. Michael, Local mechanical properties of dissimilar metal TIG welded joints of CoCrFeMnNi high entropy alloy and AISI 304 austenitic steel. Weld World. **68**(6), 1563–1573 (2024). https://doi.org/10.1007/s40194-024-01718-4
41. T. Richter, K. Erxleben, M. Rhode, D. Schroepfer, T. Michael, A. Boerner, Microstructure characterization of dissimilar metal welds of innovative high- and medium-entropy alloys to austenitic stainless steels joint by tungsten inert gas and friction stir welding. Weld World. **68**, 557–565 (2023). https://doi.org/10.1007/s40194-023-01618-z
42. P. Zhang, Y. Qi, Q. Cheng, X. Sun, Welding dissimilar alloys of CoCrFeMnNi high-entropy alloy and 304 stainless steel using gas tungsten arc welding. J. Mater. Eng. Perform. **33**(7), 3273–3282 (2024). https://doi.org/10.1007/s11665-023-08229-1
43. H. Do, S. Asadi, N. Park, Microstructural and mechanical properties of dissimilar friction stir welded CoCrFeMnNi high entropy alloy to STS304 stainless steel. Mater. Sci. Eng. A **840**, 142979 (2022). https://doi.org/10.1016/j.msea.2022.142979
44. J. Zhang, H. Lv, S. Yan, R. Fu, Y. Li, Microstructure and cryogenic mechanical properties of dissimilar friction stir welding joints between nitrogen-alloyed CoCrFeMnNi high-entropy alloy and high-manganese austenite steel. J. Mater. Res. Technol. **32**, 4059–4068 (2024). https://doi.org/10.1016/j.jmrt.2024.08.184
45. A. O'Brien, C. Guzman (eds.), *Welding Handbook. Vol. 3: Welding Processes, Part 2*, 9th edn. (American Welding Soc, Miami, 2007)
46. Y. Liu, Y. Luo, D. Zhao, G. Zhang, L. Kang, Interfacial behavior and joint performance of high-entropy alloy CoCrFeMnNi and pure Cu joints obtained by vacuum diffusion welding. J. Mech. Eng. **53**(2), 84 (2017). https://doi.org/10.3901/JME.2017.02.084
47. H. Sun, N. Hashimoto, H. Oka, Vacuum diffusion bonding between equiatomic CoCrNi-based concentrated solid solution alloys system and 316 stainless steel by spark plasma sintering. Mater. Sci. Eng. A **879**, 145297 (2023). https://doi.org/10.1016/j.msea.2023.145297
48. H. Gao et al., Diffusion bonding of high entropy alloy and stainless steel at a relative lower temperature via surface nano-crystallization treatment. J. Mater. Res. Technol. **24**, 475–487 (2023). https://doi.org/10.1016/j.jmrt.2023.03.026
49. O.B. Nenuwa, L. Thiercelin, L. Peltier, E. Fleury, N. Siredey-Schwaller, A. Benaarbia, Dissimilar diffusion welding of some equiatomic FCC-structured CoCrFeNi-based binary and multi-component alloys to 316L stainless steel. Mater. Charact. **226**, 115173 (2025). https://doi.org/10.1016/j.matchar.2025.115173
50. M.C. Harold (ed.), *Steel Products Manual: Stainless Steels* (Iron & Steel Society, Warrendale, 1999)
51. N.F. Kazakov (ed.), *Diffusion Bonding of Materials*, 1st edn. (Pergamon Press, Oxford, 1985)
52. M. Kumaran, T. Sathies, N.S. Balaji, G. Bharathiraja, S. Mohan, V. Senthilkumar, Influence of heat treatment on stainless steel 316L alloy fabricated using directed energy deposition. Mater. Today: Proc. **62** 5307–5310 (2022). https://doi.org/10.1016/j.matpr.2022.03.380
53. K.-Y. Tsai, M.-H. Tsai, J.-W. Yeh, Sluggish diffusion in Co–Cr–Fe–Mn–Ni high-entropy alloys. Acta Mater. **61**, 4887–4897 (2013). https://doi.org/10.1016/j.actamat.2013.04.058
54. W. Kucza, J. Dąbrowa, G. Cieślak, K. Berent, T. Kulik, M. Danielewski, Studies of sluggish diffusion effect in Co-Cr-Fe-Mn-Ni, Co-Cr-Fe-Ni and Co-Fe-Mn-Ni high entropy alloys; determination of tracer diffusivities by combinatorial approach. J. Alloys Compd. **731**, 920–928 (2018). https://doi.org/10.1016/j.jallcom.2017.10.108
55. J. Dąbrowa, W. Kucza, G. Cieślak, T. Kulik, M. Danielewski, J.-W. Yeh, Interdiffusion in the FCC-structured Al-Co-Cr-Fe-Ni high entropy alloys: experimental studies and numerical simulations. J. Alloys Compd. **674**, 455–462 (2016). https://doi.org/10.1016/j.jallcom.2016.03.046
56. M. Vaidya, K.G. Pradeep, B.S. Murty, G. Wilde, S.V. Divinski, Bulk tracer diffusion in CoCrFeNi and CoCrFeMnNi high entropy alloys. Acta Mater. **146**, 211–224 (2018). https://doi.org/10.1016/j.actamat.2017.12.052
57. M.A. Meyers, K.K. Chawla, *Mechanical Behavior of Materials*, 2nd edn. (Cambridge University Press, Cambridge, 2009)
58. R. Song, J. Xiang, D. Hou, Characteristics of mechanical properties and microstructure for 316L austenitic stainless steel. J. Iron Steel Res. Int. **18**(11), 53–59 (2000). https://doi.org/10.1016/S1006-706X(11)60117-9
59. S. Kheiri, H. Mirzadeh, M. Naghizadeh, Tailoring the microstructure and mechanical properties of AISI 316L austenitic stainless steel via cold rolling and reversion annealing. Mater. Sci. Eng. A **759**, 90–96 (2019). https://doi.org/10.1016/j.msea.2019.05.028
60. J.K. Stanley, A.J. Perrotta, Grain growth in austenitic stainless steels. Metallography. **2**, 349–362 (1969). https://doi.org/10.1016/0026-0800(69)90065-2
61. J. Gilewicz-Wolter, J. Dudała, Z. Żurek, M. Homa, J. Lis, M. Wolter, Diffusion of chromium, manganese, and iron in MnCr2O4 spinel. J Phs Eqil and Diff. **26**(5), 561–564 (2005). https://doi.org/10.1007/s11669-005-0051-2
62. F.H. Stott, F.I. Wei, C.A. Enahoro, The influence of manganese on the high-temperature oxidation of iron-chromium alloys. Mater. Corros. **40**(4), 198–205 (1989). https://doi.org/10.1002/maco.19890400403
63. J. Yan, X. Huang, W. Huang, High-temperature oxidation behavior of 9Cr-5Si-3Al ferritic heat-resistant steel. Int. J. Miner. Metall. Mater. **27**(9), 1244–1250 (2020). https://doi.org/10.1007/s12613-019-1961-z
64. W.-M. Choi, Y.H. Jo, S.S. Sohn, S. Lee, B.-J. Lee, Understanding the physical metallurgy of the CoCrFeMnNi high-entropy alloy: an atomistic simulation study. Npj Comput. Mater. **4**(1), 1 (2018). https://doi.org/10.1038/s41524-017-0060-9
65. T.R. Paul, I.V. Belova, G.E. Murch, Analysis of diffusion in high entropy alloys. Mater. Chem. Phys. **210**, 301–308 (2018). https://doi.org/10.1016/j.matchemphys.2017.06.039

66. M. Vaidya, S. Trubel, B.S. Murty, G. Wilde, S.V. Divinski, Ni tracer diffusion in CoCrFeNi and CoCrFeMnNi high entropy alloys. J. Alloys Compd. **688**, 994–1001 (2016). https://doi.org/10.1016/j.jallcom.2016.07.239
67. J. Kottke et al., Tracer diffusion in the Ni–CoCrFeMn system: transition from a dilute solid solution to a high entropy alloy. Scripta Mater. **159**, 94–98 (2019). https://doi.org/10.1016/j.scriptamat.2018.09.011
68. S.V. Divinski, A.V. Pokoev, N. Esakkiraja, A. Paul, A mystery of sluggish diffusion in high-entropy alloys: the truth or a myth?. Diffus. Found. **17**, 69–104 (2018 https://doi.org/10.4028/www.scientific.net/DF.17.69
69. Y.J. Fang, X.S. Jiang, D.F. Mo, T.F. Song, Z.P. Luo, Microstructure and mechanical properties of the vacuum diffusion bonding joints of 4J29 kovar alloy and 316L stainless steel using pure cobalt interlayer. Vacuum. **168**, 108847 (2019). https://doi.org/10.1016/j.vacuum.2019.108847
70. M. Samiuddin, J. Li, M. Muzamil, S. Uddin, J. Xiong, Mechanical and microstructural characterization of the bond interface formed in diffusion welding of CoCrNi medium entropy alloy (MEA) and AISI 304 stainless steel under various processing parameters. Met. Mater. Int. **29**(5), 1421–1440 (2023). https://doi.org/10.1007/s12540-022-01309-2
71. C. Velmurugan, V. Senthilkumar, S. Sarala, J. Arivarasan, Low temperature diffusion bonding of Ti-6Al-4V and duplex stainless steel. J. Mater. Process. Technol. **234**, 272–279 (2016). https://doi.org/10.1016/j.jmatprotec.2016.03.013
72. J. Jaseliunaite, A. Galdikas, Kinetic modeling of grain boundary diffusion: the influence of grain size and surface processes. Materials. **13**(5), 1051 (2020). https://doi.org/10.3390/ma13051051